Icarus 333 (2019) 516–527

Contents lists available at ScienceDirect

Icarus

journal homepage: www.elsevier.com/locate/icarus

Reflectance spectra of seven lunar swirls examined by statistical methods: A space weathering study

Kateřina Chrbolková[a,b,*], Tomáš Kohout[a,c], Josef Ďurech[b]

[a] Department of Geosciences and Geography, Faculty of Science, University of Helsinki, Gustaf Hällströmin katu 2, 00560 Helsinki, Finland
[b] Astronomical Institute, Faculty of Mathematics and Physics, Charles University, V Holešovičkách 2, 18000 Prague, Czech Republic
[c] Institute of Geology, The Czech Academy of Sciences, Rozvojová 269, 16500 Prague, Czech Republic

ARTICLE INFO

Keywords:
Space weathering
Moon
Surface
Lunar swirls
Spectra
Principal component analysis

ABSTRACT

Higher magnetic field in lunar swirls is believed to deflect majority of incoming charged particles away from the lunar-swirl surfaces. As a result, space weathering inside and outside swirls should be different. We wanted to evaluate these differences, therefore we have examined seven swirl areas on the Moon (four mare and three highland swirls). We applied the Modified Gaussian Model to statistical sets of the Moon Mineralogy Mapper spectra. Using Principal Component Analysis (PCA), we were able to distinguish the old (weathered) material from both the fresh crater and swirl materials. The swirls did not follow the same behavior as the fresh material, nor were they fully separable. Additionally, we could distinguish between the mare and highland swirls (mare/highland dichotomy) based on the PCA and histogram plots of the albedo and strength of the 1000-nm absorption band. The mare/highland dichotomy can partially be caused by different FeO content in maria and highlands, which points to the existence of a threshold value that changes the spectral evolution due to space weathering. Slope behavior seemed to be dependent on whether the swirl was on the near- or far-side of the Moon, likely due to shielding of lunar nearside by Earth's magnetotail. Our results thus favor the solar wind stand-off hypothesis in combination with the fine dust transport hypothesis and point to the fact that micrometeoroid impacts generally do not reproduce the same weathering trends as all the space weathering effects together.

1. Introduction

1.1. Space weathering

Our knowledge of the mineralogy of most of the small Solar System bodies is in some cases based on meteorite falls (Shestopalov et al., 2010), and sample-return missions such as the Hayabusa (Mikouchi et al., 2014) and the Stardust mission (Simon et al., 2008), or currently operating Hayabusa 2 (Tsuda et al., 2013) and OSIRIS-REx missions (Lauretta et al., 2017). However, in most cases, we are still dependent on remotely measured reflectance spectra (Gaffey et al., 1993; Shuai et al., 2013). A spectrum of an airless planetary body is controlled by surface properties, which are influenced by so-called *space weathering* (i.e., Hapke, 2001). The term space weathering describes how a set of effects, including the solar wind, galactic radiation, and micrometeoroid impacts causes chemical and physical changes to the airless planetary surfaces. Among other changes such as formation of agglutinates and blistering, space weathering creates small particles of metallic iron (so-called nanophase iron, npFe^0) in thin rims of regolith grains, which diminish the albedo, spectral contrast (absorption band depth), and increase the spectral slope (Hapke, 2001; Matsumoto et al., 2015; Pieters and Noble, 2016; Pieters et al., 2000). These effects complicate our interpretation of mineralogy.

As Pieters et al. (2000) pointed out, space weathering is a complicated problem because the different effects causing the spectral changes vary with location in the Solar System. Another important factor is mineralogy, especially the amount of iron in silicates. The more iron present in the silicate material, the more efficiently is the nanophase iron produced. A relationship between the size of the npFe^0 particles and the spectral changes was reviewed for example by Blewett et al. (2011).

Several works described how the whole set of processes (solar wind and micrometeoroid impacts) influence the spectra of airless bodies (for example Hapke, 2001; Pieters et al., 2000). Noguchi et al. (2011) studied particles from the asteroid Itokawa and concluded that typical timescales of the solar wind weathering are 10^4 to 10^6 years, whereas in

* Corresponding author at: Gustaf Hällströmin katu 2 (Physicum), P.O. Box 64, FI-00014 University of Helsinki, Finland.
E-mail address: katerina.chrbolkova@helsinki.fi (K. Chrbolková).

https://doi.org/10.1016/j.icarus.2019.05.024
Received 1 November 2018; Received in revised form 16 May 2019; Accepted 20 May 2019
Available online 29 May 2019

the case of micrometeoroid impacts it is longer, 10^8 to 10^9 years. Also, Sim et al. (2017) reported a variation in crater-walls' weathering, which they prescribed to a differing solar wind flux due to passage of the Moon through the Earth's magnetotail. Similar conclusions were made by Hemingway et al. (2015) based on latitudinal variations of the spectra across the lunar maria. However, the exact description of these changes is still lacking, and we cannot assign a specific change in the spectra to a specific weathering process.

1.2. Lunar swirls

Very valuable natural laboratories for space weathering studies are the so-called *lunar swirls*. Lunar swirls are areas on the Moon that have brighter albedo, and are usually of a curved shape (Blewett et al., 2011; Hood et al., 1979a; (Hood and Williams, 1989). All known swirls lie in places of amplified magnetic field (Blewett et al., 2011; Hood et al., 1979a; Hood et al., 1979b) and many of them are antipodal to major impact basins (Hood and Artemieva, 2008). An example of a lunar swirl is the Gerasimovich anomaly – which is also an area of the strongest magnetic field on the Moon – or other well-known swirls such as Reiner Gamma or Mare Ingenii (Blewett et al., 2011).

Origin of lunar swirls

One of the main hypotheses for formation of lunar swirls is that amplified magnetic field shields surface of swirls from solar wind and so space weathering is diminished in them and they look fresh (herein referred to as the solar wind stand-off hypothesis; Deca et al., 2018; Glotch et al., 2015; Hemingway and Garrick-Bethell, 2012; Hood and Schubert, 1980). The idea of charged particles being deflected away from lunar swirl areas was described for example by Hood and Williams (1989). This hypothesis is often connected to the antipodal hypothesis, which prescribes the origin of a magnetic anomaly to a collision of ejecta from an impact creating an antipodal basin Hood et al. (2001). This hypothesis correlates with recent study done by Kelley and Garrick-Bethell (2019), who found that the magnetic anomalies in the Gerasimovich region are offset to the west with respect to the Crisium antipode, which in accordance with the slight rotation of the Moon during the ejecta's circulation around the Moon. Although, not all lunar swirls are in the positions antipodal to some impact basin. Magnetic-field measurements done by Lunar Prospector mission support the validity of the solar wind stand-off hypothesis in the Imbrium antipode (Lin et al., 1998).

Another option proposed at approximately same time as the solar wind stand-off hypothesis is a hypothesis of relatively recent impacts of a system of comets onto the surface of the Moon (Schultz and Srnka, 1980; Syal et al., 2015). In the place of the impact, turbulent flows of cometary coma should have (1) heated the material above the Curie temperature, which caused magnetization of the surface; (2) deposited or altered the top-most regolith layer. This alteration would result in distinct surface roughness in the swirl area (Pinet et al., 2000), but such option was mostly ruled out by the Diviner and Mini-RF data (Glotch et al., 2015; Jozwiak and Blewett, 2017; Kramer et al., 2011a) as the swirls have similar cm-scale roughness as their surroundings.

Garrick-Bethell et al. (2011) suggested that lunar swirls are bright thanks to an accumulation of fine feldspathic (bright) regolith in swirl areas. Based on the theory, the fine fraction of regolith should be electrostatically lofted during terminator crossings, and transported by weak electric potentials that are created in the vicinity of swirls. Alternatively, nearby impacts could have distributed fine material over large areas – even to swirls and they thus look fresh.

Despite the previous research, the origin of swirls is still unknown and it is possible that they were formed and still look fresh due to a combination of the above-mentioned effects.

1.3. Multispectral datasets

This work uses a multispectral dataset, as it has the potential to support us with valuable information concerning space weathering and lunar research. For example analysis of data from the Clementine probe by Blewett et al. (2005) showed that the Descartes swirl is probably an ejecta material from the two nearby craters, which has high albedo due to lower maturity. Later, Blewett et al., (2011) presented other results based on Clementine dataset, suggesting that swirls have spectral characteristics of immature material. Their findings contradict the cometary hypothesis, but are in accordance with the solar wind stand-off hypothesis and the dust-levitation hypothesis. Kramer et al. (2011b) showed, on spectra from small craters in lunar-swirls' areas, that swirls are not immature, even though they look fresh. Based on the Clementine data, latitudinal variation in spectral properties of lunar maria (that match the situation in lunar swirls) was shown by Hemingway et al. (2015). This result is in favor of the solar wind flux reduction in the swirls' areas as proposed by the stand-off hypothesis.

The Moon Mineralogy Mapper (M^3) spectra can be used to identify fresh craters, as shown by Nettles et al. (2011). They used the spectra to evaluate the maturity trends in fresh craters and their rays. Kramer et al. (2011a) also used the M^3 dataset, specially in areas of three lunar swirls (Reiner Gamma, Gerasimovich, and Mare Ingenii), to evaluate the characteristics of fresh craters and mature soils, and on- and off-swirl trends. They found that on-swirl craters have higher albedo and more intense absorption features than off-swirl craters. They also proposed that the maturation process is retarded inside swirls because the solar wind ions are deflected to adjacent areas, which are, on the other hand, more weathered.

Denevi et al. (2014), using data from the Lunar Reconnaissance Orbiter's Wide Angle Camera, pointed out that the spectral slope in the ultraviolet wavelength range is decreasing not increasing with maturation.

Very recent work by Trang and Lucey (2019) used data from the Kaguya Multiband Imager and mapped the abundance of different sizes of nanophase iron across the lunar swirl areas.

Not only the Moon was spectrally measured, the Itokawa asteroid's multispectral data showed that the darker areas have usually spectra with higher spectral slope (Hiroi et al., 2006) and that the albedo vary from the regions that are expected to be fresh (such as crater walls) to the mature regions (Ishiguro et al., 2007).

Our goal is to determine the spectral characteristics of the swirl material in comparison with fresh (crater) material and old (weathered, mature) material by deliberate targeted selection of statistical sets of spectral data, which is a different approach to previous works done for example by Kramer et al. (2011a) or Trang and Lucey (2019) who mapped whole areas of swirls at once or chose only few points to compare the spectral characteristics. This is how we want to evaluate how the swirl material behaves and to get some clue on which hypothesis explaining swirl immaturity is the more probable one. If the solar wind stand-off hypothesis is correct, soils inside the swirl are affected mainly by micrometeoroid impacts and we should be able to identify how micrometeoroids influence the spectral trends compared to the complete weathering in the surrounding material and fresh crater material. Thus, we propose our main hypothesis: the sequence of values of a given spectral parameter, should be as follows: **crater → swirl → mature material**. In other words, our central hypothesis is that swirl material should exhibit intermediate behavior with respect to fresh crater material and mature terrains due to smaller amount of effects causing the space weathering.

In this article, we analyze spectra of seven lunar swirl areas: Reiner Gamma, Rima Sirsalis, Mare Marginis, Mare Ingenii, Airy, Descartes, and Gerasimovich. The first four represent mare swirls, the remaining three are highland swirls. The Rima Sirsalis swirl was proposed to be a part of the Reiner Gamma formation by Hood et al. (2001). Lee et al. (2019) supported this idea as they found that the magnetizations of

these two swirls are aligned. However, their distance is larger than 200 km and Rima Sirsalis is nearer to the highland regions than Reiner Gamma, we thus analyze them separately.

2. Choice of the data and methods

For our work, we used lunar spectra (Section 2.1), which we processed with an adaptation of the Modified Gaussian Model (MGM) (Sunshine et al., 1990; Sunshine et al., 1999), see Section 2.2. With this model, we got three major spectral parameters: the spectral slope, albedo, and strength of the 1000-nm band. We applied three different approaches to analyze our data/spectral parameters (histogram plots, spectral stacking, and Principal Component Analysis, described in Section 2.3). Original data, files with results, and our MATLAB code are available at https://doi.org/10.5281/zenodo.1473816.

2.1. Datasets

A list of the swirls we used for this study is at the end of Section 1. We have chosen these seven swirls in order to cover different locations on the Moon (the near and far side, northern and southern hemisphere, etc.). The main constraints were: good-quality coverage of the swirl by spectral data, nearly homogeneous surface mineralogy, and not very diverse geological settings in the area of the given swirl and its close vicinity.

Spectra were recorded in the years 2008 to 2009 by the Moon Mineralogy Mapper (M^3) carried by the Chandrayaan-1 spacecraft (Green et al., 2011). M^3 captured 95% of the lunar surface in two mapping modes. We use data from the “Global Mode” (more precisely Level 2 reflectance data), as they covered a much larger area. This mode obtains 83 spectral channels ranging from 541 to 2976 nm. Each spectrum was thermally (Clark et al., 2011) and photometrically corrected (Besse et al., 2013).

We downloaded the spectral cubes from the Planetary Data System, Geosciences Node[1] (see the Online Supplementary Material, Table S1, for a list of spectral cubes and positions of the areas we used), and then chose spectra for our analysis with the ENVI software. Before further processing, we normalized the spectra at 750 nm.

In each swirl, we visually identified four distinct terrains: (1) fresh crater material outside the swirl formation (in this article marked as *fresh out*), (2) fresh crater material inside the swirl (*fresh in*), (3) swirl material that is distant from the fresh craters (*mature in*), and (4) old weathered material outside the swirl distant from any fresh crater (*mature out*). For each terrain of a given swirl, we chose several tens to hundreds of spectra. The number was dependent on the availability of spectral data for a given type of terrain. We have chosen spectra so that the given terrain is represented by several areas latitudinally and longitudinally spread over the swirl. The fresh craters were identified by the visual presence of the sharp rays, and we chose spectra that were outside the center of the crater but not too far from it to avoid possible mixing with the background mature material. Especially in the highland regions, the identification of the *fresh in* and *fresh out* terrains was more demanding because of the lower albedo contrast of the material, see Fig. 1. The total number of spectra for each swirl are as follows: Reiner Gamma (1324), Rima Sirsalis (179), Mare Ingenii (600), Mare Marginis (887), Airy (538), Descartes (1056), and Gerasimovich swirl (829).

2.2. Adaptation of MGM

The Modified Gaussian Model (MGM) for fitting olivine and pyroxene mineral absorption spectra was developed by Sunshine et al. (1990) and further distributed in several formats (Sunshine et al., 1999). We used the codes written in MATLAB. MGM generally fits an input spectrum as a sum of a polynomial-shaped continuum and a given number of absorption bands represented by modified[2] Gaussian distributions, see (Sunshine et al., 1990). The fit is done in the natural logarithm of reflectance, $\ln(R)$, and energy, $1/\lambda$, as this allows for a simple mathematical summation of the absorption bands and continuum. The main reason for the choice of these variables is the existence of the Lambert-Beer's law explaining relation between the reflectance and exponential of the absorption coefficient, thus natural logarithm of reflectance and sum of individual absorption features.

Sunshine et al. (1990) originally produced a code that works in an interactive way, enabling a user to fit one spectrum at a time. We wanted to treat several tens to hundreds of spectra in one run. Thus, we developed a simple routine that estimated input parameters to MGM for each individual spectrum:

1. We fitted the overall continuum (the wavelength range was from approximately 660 nm to 2936 nm) by a linear function to obtain the estimates of the offset and slope of the continuum.
2. We fitted the 1000- and 2000-nm absorption bands by second-order polynomials.
3. A difference between the reflectance value at a given wavelength in the 1000- and 2000-nm band and the corresponding reflectance of the continuum fitted in the area of the band (local continuum), gave estimates of the absorption bands' strengths.
4. A parallel line to the local continuum over the band in one half of the depth of the band, supplied us with the Full Width at Half Maximum (FWHM). Where the line intersected the band's fit from point 2, we marked two points. Their wavelength difference was FWHM.
5. We had a minimum of two[3] absorption bands (at 1000 and 2000 nm), the third band around 1200 nm was added when the angle between the continuum and a straight-line fit of the 1200-nm region was above a certain value (0.55 rad). We added the fourth band at 3000 nm based on its visual presence, which only happened when we used the stacking method (Section 2.3.2) and we did not evaluate the parameters of this band.
6. When we had the input parameters, we ran MGM to get the optimized spectral parameters.

For an illustration of these steps see Fig. 2. Our estimation routine significantly improved the ability of MGM to converge to physically realistic solutions.

The 1000-nm absorption band in our spectra is probably caused by electron excitations of Fe^{2+} ions in M_2 positions in pyroxenes (Burns, 1989). Partial contribution to this band can also have olivine, which creates a broad absorption around 1000 nm that is made of three bands due to electron excitations in Fe^{2+} ions in M_2 (strong central absorption) and M_1 (weaker absorptions and shoulders) sites (Burns, 1970). The M^3 data are not of good enough quality for us to have a unique solution with three bands, though. Therefore, we used only one band to have the model constrained. Klima et al. (2007) showed that the 1200-nm band is caused by Fe^{2+} ions in M_1 sites in pyroxenes and its intensity is higher the higher is the iron content of the pyroxene.

2.3. Methods

We followed three different approaches: statistical evaluation of our results using histogram plots (Section 2.3.1), spectral stacking (Section 2.3.2), and the Principal Component Analysis (Section 2.3.3).

[1] http://ode.rsl.wustl.edu/moon/index.aspx

[2] Modification allows for asymmetric appearance of the Gaussian curve.

[3] With the exception of the Descartes swirl, where we were unable to detect the 1000-nm band.

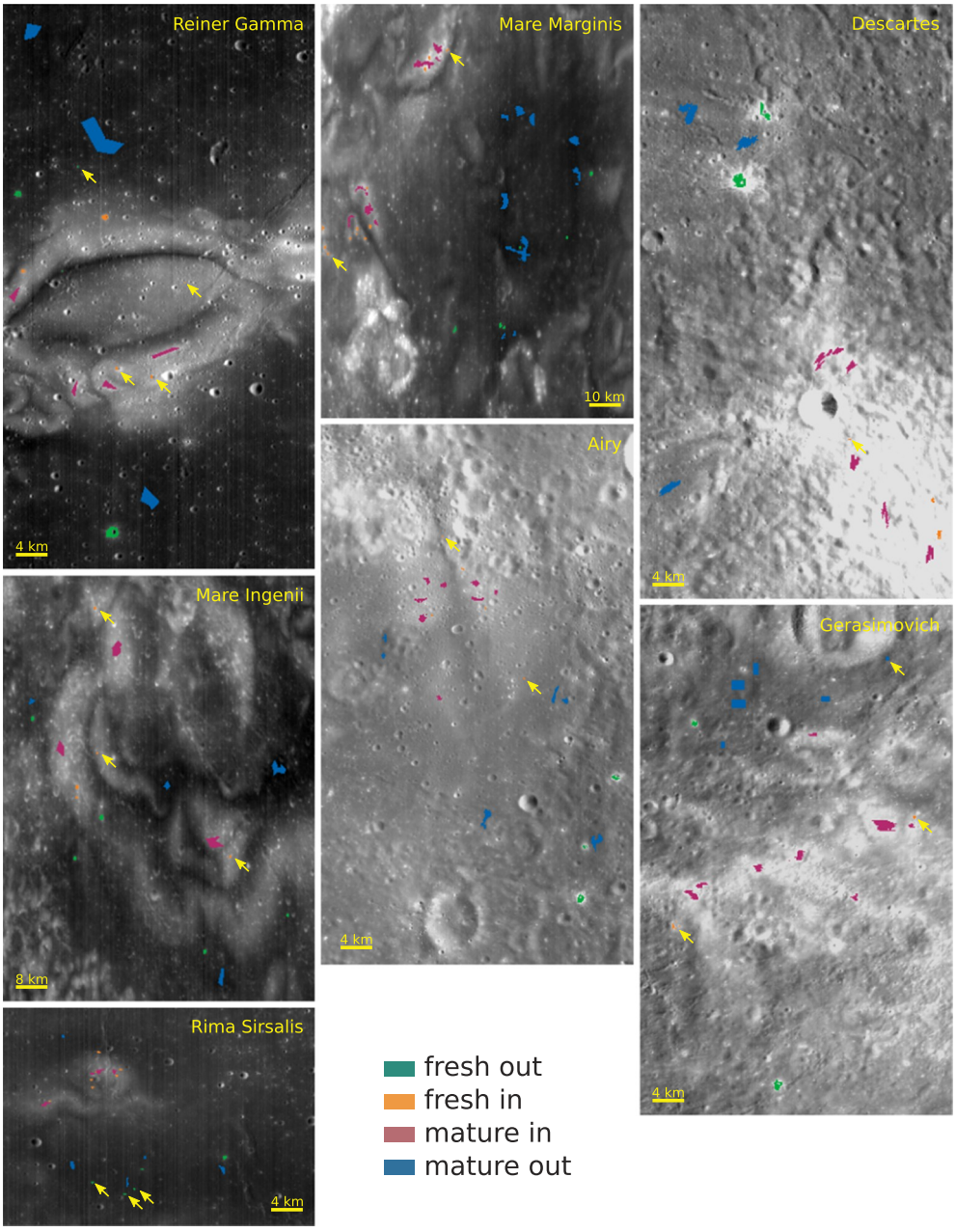

Fig. 1. Swirls from this study shown as 750-nm reflectance images with highlighted pixels of the Moon Mineralogy Mapper's spectra we used for our analysis. Each terrain has a different color (color-coding is consistent throughout the whole article). Groups of only few pixels that are difficult to be seen were additionally marked by yellow arrows to increase their visibility. All images have adjusted contrast and brightness to enable easier identification of locations of pixels we used. For coordinates of centers of individual images in the mosaic see the Online Supplementary Material, Table S1; for individual images, see Figs. S1 to S7. (For interpretation of the references to color in this figure legend, the reader is referred to the web version of this article.)

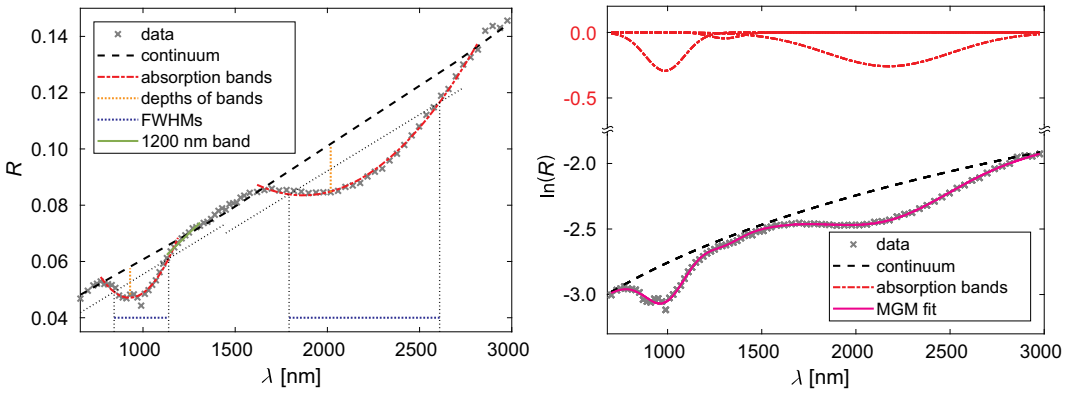

Fig. 2. (left) An output plot of our routine for estimation of input parameters to MGM. The wavelength is denoted λ, *R* stands for the reflectance. The spectrum belongs to fresh Reiner Gamma crater material outside the swirl (*fresh out*). (right) An optimized fit done in MGM based on the input parameters from our routine.

2.3.1. Histogram plots

In the first approach, we took all the spectra from a given terrain in a swirl and fitted them with MGM. This gave us four statistical sets (for four terrains in one swirl) of the spectral parameters important for our space weathering study (namely the spectral slope, albedo,[4] and strength of the 1000-nm band). Although we fitted the 2000-nm band, we did not evaluate its strength because of the lower quality of the data at longer wavelengths, caused by the imperfect thermal correction and higher relative noise influencing the depth estimate.

When we had all the fits, we created a histogram plot (using the Probability density function normalization and Sturges' binning algorithm, Sturges, 1926) of the four statistical sets/terrains of the given swirl, which we further evaluated using the terrains' mean values. To test our hypothesis about the intermediate behavior of swirl material (Section 1), we analyzed the sequence of the four means of the chosen spectral parameter. We had to assess if this sequence is statistically unambiguous (two means do not switch their positions with a slight change of the dataset). Thus, we proposed a null hypothesis: *The two tested mean values are the same*. To test the null hypothesis, we used the Two-sample t-test with a significance level of 5% (see also Section 3.1 for an illustration of our approach).

2.3.2. Spectral stacking

Another approach was to take all the spectra from a given terrain of one swirl and stack (sum) them. This created one representative spectrum of the terrain (an alternative to an average spectrum), which was of better quality than each of the previous spectra, as the noise was subdued.

We then fitted the four stacked spectra (of four terrains) for each swirl with MGM, and compared the output parameters.

2.3.3. Principal Component Analysis

The third approach was based on the Principal Component Analysis (PCA), which is a linear transformation that reduces the dimensionality of a problem (Connolly and VanderPlas, 2014). In our case, 83 reflectance values for several hundreds of spectra (n), created an $83 \times n$-dimensional space (cloud of points). PCA takes this cloud and rotates its axes to get the maximum variance in the data explained by a smaller number of variables than the original 83. These new variables are called the principal components. The first principal component (PC1) usually explains the maximum variance given by the overall shape of the data cloud. Orthogonal to the PC1 and in a direction of the biggest variance that remained in the data lies the second principal component (PC2). Higher order principal components explain finer structures in the data up to the residual noise. PCA therefore separates valuable information into the first few components.

We still have to bear in mind that PCA is a mathematical apparatus enabled mainly by matrix operations (for example see Jolliffe, 2002, for more details). The results we obtain by this method have therefore rather abstract meaning. It is not always[5] possible to assign a specific physical variable to the given principal component and vice versa. Nevertheless, PCA is useful to reveal significant trends in the data. An illustration can be a robust asteroid taxonomy, based on the relative positions in the principal-component space, see (DeMeo et al., 2009).

Before entering the data into the PCA, we divided the values from each spectral band by their variance (in accordance with Connolly and VanderPlas, 2014), to make sure that the variations in the data are comparable. For the PCA, we subtracted the mean from all the data in a given spectral band.

PCA on whole regions of lunar swirls, without distinction of the different terrains, had already been applied by Kramer et al. (2011a).

[4] Albedo was evaluated from non-normalized spectra at 1500 nm.

[5] In case of asteroid families, PC1 correlates significantly with the average spectral slope, and thus with the age of the family (Nesvorný et al., 2005).

3. Results

3.1. Results of histogram plots and spectral stacking

Applying the methods from Section 2.3.1, we got three histograms for each swirl (for distributions of the albedo A, slope s, and strength of the 1000-nm band S_{1000} in different terrains), see Fig. 3 for an example, and the Online Supplementary Material, Figs. S8 to S10 for the rest of the histograms.

Based on the procedure described in Section 2.3.2, we created the stacked spectra. See Fig. 4 for all the stacked spectra from all our swirls.

Based on histograms (Fig. 3 and S8 to S10), we noticed that for some swirls the *mature in* material had a mean value in between the fresh material and *mature out* material. This supported our hypothesis about the intermediate behavior of the *mature in* terrain (see end of Section 1). In other cases, the swirl material (*fresh in* and *mature in*) and the non-swirl material (*fresh out* and *mature out*) clustered together. We also observed these trends in the data from the stacking method. See Table 1 for an overview of the results of the null-hypothesis testing (Section 2.3.1) for both histograms and stacking methods. In the table, "✓" means that the null hypothesis was rejected and there was a clear sequence of mean values: *fresh in, fresh out* → *mature in* → *mature out*, agreeing with our central hypothesis. Usually, it was enough to test only one mean-value pair of distributions/terrains, as the rest of the pairs in the histogram were clearly and significantly ordered. This situation is depicted in Fig. 3 (left). The "×" symbol represents rejection of the null hypothesis in cases where the sequence of the mean values was unambiguous but did not follow our theory, such as the situation in Fig. 3 (right). When the null hypothesis could not be rejected, at the 5% significance level, the table shows "○". We notice several things based on the table:

Albedo: The highland swirls followed our theory of intermediate behavior for albedo, whereas in the mare swirls, the *mature in* terrain had higher albedo than the *fresh out* material.
Slope: We noticed that in case of slope, swirls that are found at the nearside of the Moon (Reiner Gamma, Rima Sirsalis, Airy, and Descartes) followed the null hypothesis, whereas the far-side swirls (Mare Ingenii and Gerasimovich) did not.
Strength: Based on the histogram results, the strength of the 1000-nm band had an inverse behavior to that described for albedo – the highland swirls did not follow the theory, but mare swirls did. The stacking results were rather insignificant in this parameter.

We also note that the Descartes swirl had an unreliably shallow 1000-nm band, if any (see Fig. 4). Therefore, we did not fit it.

Fig. 5 shows the output spectral parameters of stacked spectra with emphasis on their evolution (fresh to mature state). Based on this figure, we noticed that as material evolved from a fresh state to the weathered one, different swirls had distinct inclinations in the graph, but all were in accordance with an overall trend of decreasing albedo and depth[6] of the 1000-nm band, and increasing spectral slope. We could also see that the trend's inclination for materials inside the swirl was usually different from the trend's inclination of the materials outside it. Two observations against the usual behavior were small albedo change in the Rima Sirsalis' case and inverse behavior of the spectral slope of the Gerasimovich swirl.

3.2. Results of Principal Component Analysis

We performed the PCA (Section 2.3.3) separately for each swirl. The resulting plots, depicting the first and second principal component, can

[6] Numerical value of the strength is increasing, which means that the depth of the band is decreasing.

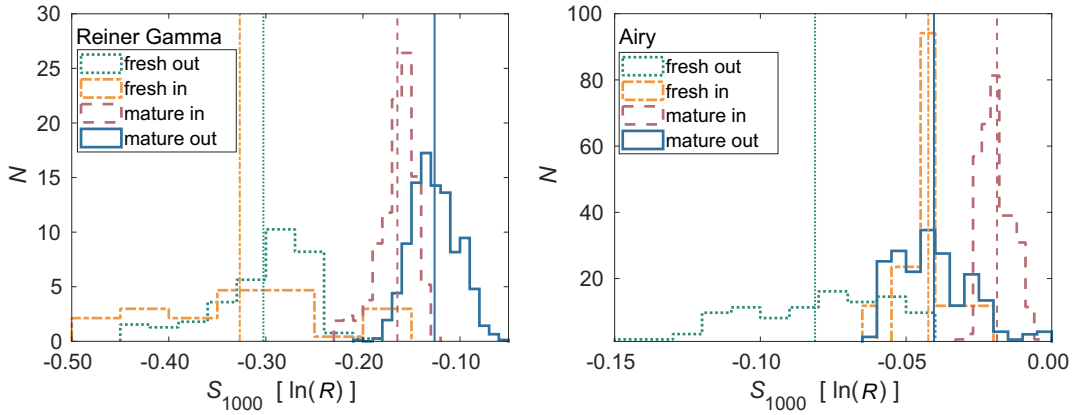

Fig. 3. An example of histograms. The left part of this figure shows a histogram of the strength of the 1000-nm band S_{1000} for the Reiner Gamma swirl. The right part is for the Airy swirl. *N* is the number of occurrences and vertical lines represent mean values. See the Online Supplementary Material, Figs. S8 to S10, for the rest of the histograms.

be found in Fig. 6. This figure also shows, for each swirl, four additional points, which represent the swirl's stacked spectra. We calculated their position in the principal-component space after the main PCA run.

Looking at Fig. 6, we noticed that the *mature out* material could always be distinguished from the other three terrains. Whereas the *mature in* material had variable positions with reference to the fresh materials. As we expected, the *fresh in* and *fresh out* terrains usually occupied the same region of the principal component space. Additional points from stacking usually lay in the middle of the statistical cloud corresponding to the same terrain.

We also computed the PCA for all the swirls together. Spectra belonging to one terrain were represented by the same marker. The final graph, Fig. 7, supported the previous result: the *mature out* terrain was distinct from the other terrains. This result is thus generally valid.

Fig. 8 is based on the PCA calculated only for: (a) mare swirls and (b) highland swirls. Similar figure comparing PCA for near- and far-side swirls is attached in the Online Supplementary Material (Fig. S11).

Further, we tried to evaluate correlations of individual principal components with spectral parameters, which we obtained from MGM. We found that each principal component is strongly correlated (correlation coefficient > 0.8) with more than two spectral parameters. Therefore, we did not present these results here, as they do not give any straightforward interpretation.

4. Discussion

4.1. Interpretation of space weathering trends based on PCA

The position of the *mature in* material in PC1 vs PC2 plots indicates that the swirl material is not fresh in the same way as the crater (*fresh in* and *fresh out*) material. This supports the hypothesis proposed by Pieters and Noble (2016) that the swirl material is distinct from bright soils in craters. One reason could be that the micrometeoroid impacts (presumably unaffected by the magnetic field) weather swirl material but it remains distinct from the *mature out* material, which is also intensively weathered by the solar wind that influences spectra on much shorter timescales (see Section 1.1).

We point out that lunar swirls are believed to be ≈3.8 Gyr old, thus micrometeoroid impacts should have already weathered their spectra even if they were the only agent influencing the space weathering state in the swirls (Blewett et al., 2011, and references therein), but they did not. This may point to some later alteration of the areas that would accompany the magnetic field shielding, for example deposition of fresh or bright material by electrostatic levitation or by nearby cratering events in later stages of swirls' evolution. Such idea has already been proposed for example by Hood et al. (1979b). Alternatively, the micrometeoroid impacts may influence the spectra in lunar swirls on longer timescales or differently than we have previously thought. As Trang and Lucey (2019) showed, lunar swirls are depleted in nanophase iron, but they obtain the same amount of microphase iron[7] as the rest of the area. Micrometeoroid impacts are expected to produce both, nano- and microphase iron particles (Trang and Lucey, 2019, and references therein). The relatively lower abundance of nanophase iron inside lunar swirls thus further points to the different behavior of micrometeoroid impacts in these areas. Another option – the cometary hypothesis is not very probable reason for the spectral dichotomy of the swirls because of the low probability of cometary impacts being distributed according to positions of maria and highlands and because of the near-/far-side dichotomy we discovered in the slope behavior (results of the histogram and stacking methods).

We are only showing PC1 vs PC2 plots in this article, because combinations of higher principal components did not give any significant results, due to their low variance. Still, our PCA results are very robust, because we verified that the conclusions are not sensitive to preprocessing of the spectra, or the data and quality reduction. The analysis had the same conclusions even when applied to:

- non-normalized spectra,
- spectra with subtracted continuum,
- smaller sample of spectra in each terrain,
- equivalent amounts of spectra in each terrain/swirl,
- spectra constrained to a smaller wavelength range (700–1500 nm) – see the Online Supplementary Material, Fig. S12, for an example plot,
- or output spectral parameters from our MGM routine; instead of directly inputting spectra to the PCA.

Points belonging to one terrain are sometimes divided into several clouds in principal component plots. This fact can be attributed to the selection of the data – spectra associated with one terrain originate from diverse areas over the swirl rather than from a continuous region. Also different albedo of individual swirls may play some role in case of PCAs on multiple swirls.

Some of the overlapping points that disturb the pure separation of the *mature out* material (for example in Fig. 6) can be caused by an incorrect classification of the terrains, but the overall clustering is evident even with these points.

[7] Trang and Lucey(2019) divided metallic iron particles into two groups: (1) those larger than 100 nm called microphase iron and (2) smaller than 100 nm called nanophase iron.

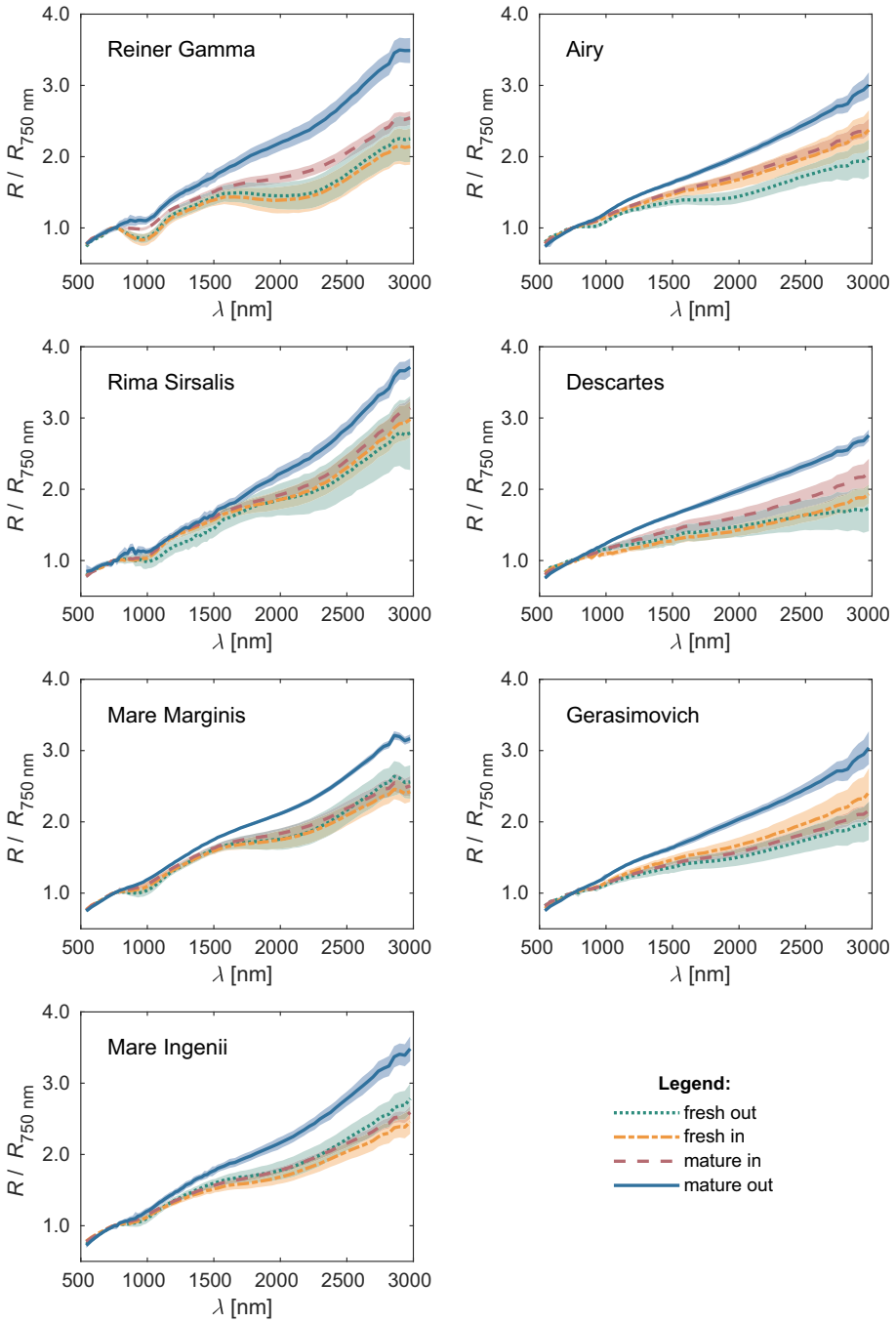

Fig. 4. Spectra of four distinct terrains in the swirls used in this work. Each line shows one representative stacked spectrum from the given terrain in the swirl. A lighter-coloured area around each line marks the one-sigma dispersion of the statistical data from which the stacked spectrum was created.

4.2. Interpretation of the mare/highland dichotomy

Table 1 shows that there is a mare/highland dichotomy in the behavior of the albedo and strength of the 1000-nm band (also Figs. S8 and S10). Mare swirls showed (Fig. S8) that the albedo when influenced predominantly by micrometeoroid impacts does not change in the same extent as if influenced by all the space weathering mechanisms. On the other hand, depth of the 1000-nm band was consistent with our null hypothesis, thus lunar swirls seemed to be in some intermediate state between fresh and mature. In highlands, the albedo behaved accordingly to our null hypothesis, but the 1000-nm band strength did not.

The principal-component plots in Fig. 6 also revealed a difference between the mare and highland swirls. The mare swirls exhibited the point-cloud's orientation dependent on both PC1 and PC2, whereas the highland-swirls' terrains did not seem to vary in PC2.

The Descartes swirl appeared intermediate, as it was also dependent on PC2, see Fig. 6. It is possible that this “non-highland” behavior is caused by the absence of the 1000-nm band, which we mentioned already in Section 2.2. Another possibility is that the Descartes swirl is not a proper type swirl, but rather crater material from two nearby craters, as previously suggested by Blewett et al. (2005). This idea could also be supported by the significant overlap of the *mature in* and *fresh in, fresh out* materials in the graph. On the other hand, Garrick-Bethell et al., (2011) showed that the spectral properties of the region are unlikely only due to craters but may be a result of the magnetic anomaly under the region. We again identified a difference in the

Table 1
Behavior of the three main spectral parameters (albedo *A*, spectral slope *s*, and strength of the 1000-nm band S_{1000}). When the mean of the swirl (*mature in*) material lies unambiguously between the *mature out* and *fresh in, fresh out* materials, "✓" (rejection of the null hypothesis) appears in the table, as in Fig. 3 (left); if the mean values' sequence is unambiguous but the swirl material does not behave intermediately, the situation is marked by "×", see Fig. 3 (right). When the null hypothesis could not be rejected, at the 5% significance level, "○" is shown in the table. Descartes did not show substantial 1000-nm band, the table thus shows "–" for this parameter. In each column, the left symbol represents the result of histogram method, the right one characterizes stacking method's results. The location column shows whether the swirl is at the near- (N) or far-side (F) or at the edge (E) of the Moon, for more precise positions of individual swirls, see the Online Supplementary Material, Table S1.

swirl	type	location	*A*	*s*	S_{1000}
Reiner Gamma	mare	N	× ×	✓ ✓	✓ ✓
Rima Sirsalis		N	× ×	✓ ✓	○ ○
Mare Marginis		E	× ×	○ ×	✓ ✓
Mare Ingenii		F	× ×	× ×	✓ ○
Airy	highland	N	✓ ✓	✓ ✓	× ○
Descartes		N	✓ ○	✓ ✓	– –
Gerasimovich		F	○ ○	× ×	× ○

the table we see that mare swirls have higher FeO content than highland swirls. One could thus say that the reason for mare/highland dichotomy is the different composition of the underlying material. Still, there is a bigger difference between individual mare swirls than between lowest mare swirl and highest highland swirl. Despite the big variation in FeO content in maria (11.5 wt%), the mare swirls behave consistently, e.g. in PCA plots, and there is a bigger difference between highlands and maria, with smaller contrast of FeO content (3.3 wt%). We thus think that there may be some additional effect influencing spectral characteristics of swirls or that there is some threshold value of FeO content that matches the dividing line between lowest mare and highest highland swirls and causes the dichotomy. Sim and Kim (2018) also observed different behavior of mare and highland craters during their analysis of Kaguya's data. Similarly, they associated trends in their dataset to varying iron content.

To find other possible causes of the mare/highland differences, we also briefly tried to compare our data to other parameters such as the altitudes of the swirls, homogeneity of the gravitational and magnetic field, magnetic field amplitude, etc., but we did not detect any correlations with them. The surface roughness distributions obtained from Mini-RF measurements of circular polarization ratio (Nozette et al., 2010) had a similar shape for all the swirls areas we used, see the Online Supplementary Material, Fig. S13. We noticed only a slight shift of the highland swirls towards higher circular polarization ratios, but not all the swirls were fully covered by the measurements. Our results of the surface roughness distributions agreed with those of Neish et al. (2011).

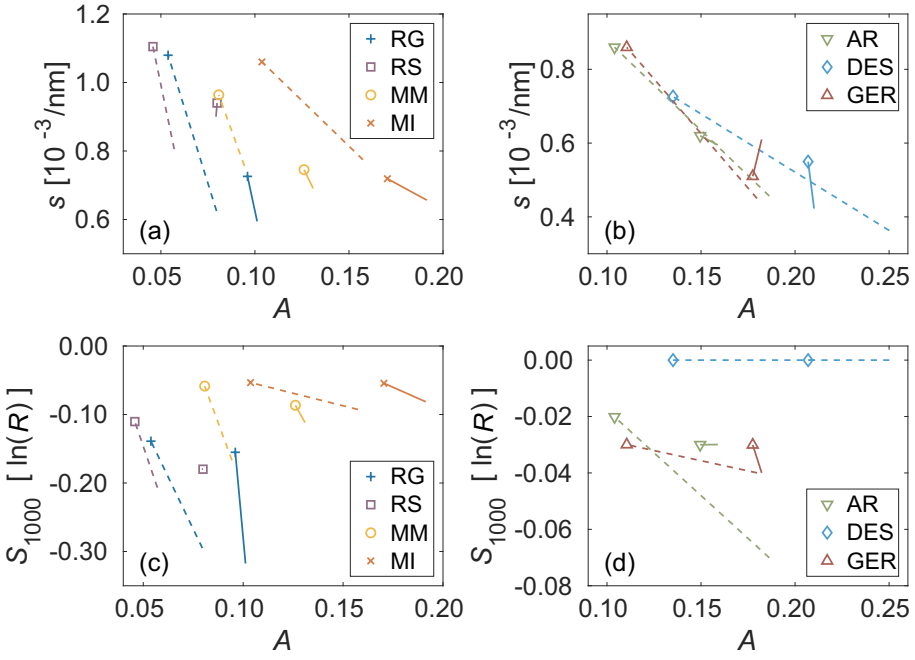

Fig. 5. The albedo *A* vs slope *s* of the (a) mare swirls, (b) highland swirls, and the albedo *A* vs strength of the 1000-nm band S_{1000} of the (c) mare swirls and (d) highland swirls. RG, RS, MM, MI, AR, DES, and GER stand for Reiner Gamma, Rima Sirsalis, Mare Marginis, Mare Ingenii, Airy, Descartes, and Gerasimovich respectively. For each swirl, there are two lines. The trend marked by a solid line represents in-swirl terrains (*fresh in, mature in*), the dashed line is for the trend outside the swirl (*fresh out, mature out* terrains). A symbol at one end of each line marks the more weathered state of that area (the dashed line goes from the fresh crater material outside the swirl (*fresh out*), to the old weathered material outside the swirl (*mature out*), marked by the symbol). The continuum was fitted in a wavelength space.

behavior of the mare and highland swirls in Fig. 8. The data from the Descartes swirl adapted to the highland-like behavior in this figure.

One reason for the difference between the mare and highland swirls can be different iron abundances in these areas (Lawrence et al., 2002), which influence the possibility of creating $npFe^0$ particles, thus the space-weathering final products. We used data from the Lunar Prospector Gamma Ray Spectrometer[8] (Prettyman et al., 2006) and estimated mean values of FeO content in the areas we used in this study, see Table 2. We divided the swirls into three groups based on their iron content: 0–7 wt% of FeO were swirls with low (L) FeO content, 7–14 wt % medium (M) FeO swirls, and > 14 wt% were swirls with high (H) content of FeO. We also verified that the distribution we obtained was in accordance with classification we would get based on the UVVIS FeO abundance from the Clementine probe data (Lucey et al., 2000). From

The mare/highland dichotomy also indicates that the origin of magnetization of the swirl area may be irrelevant to the rest of the evolution of the swirl. The Reiner Gamma swirl is not antipodal to any large impact basin, still it follows the same behavior as the Mare Ingenii and Marginis swirls, which are antipodal. Even if the mechanism creating swirls was different from the antipodal hypothesis, it would not explain the differences between maria and highlands.

Our results suggested that the albedo of the *mature in* material is higher than that of the *fresh out* terrains in mare regions, see the Online Supplementary Material, Fig. S8. A logical explanation would be that maria are usually darker than highlands. Therefore, the background

[8] http://pds-geosciences.wustl.edu/missions/lunarp/grs_elem_abundance.html

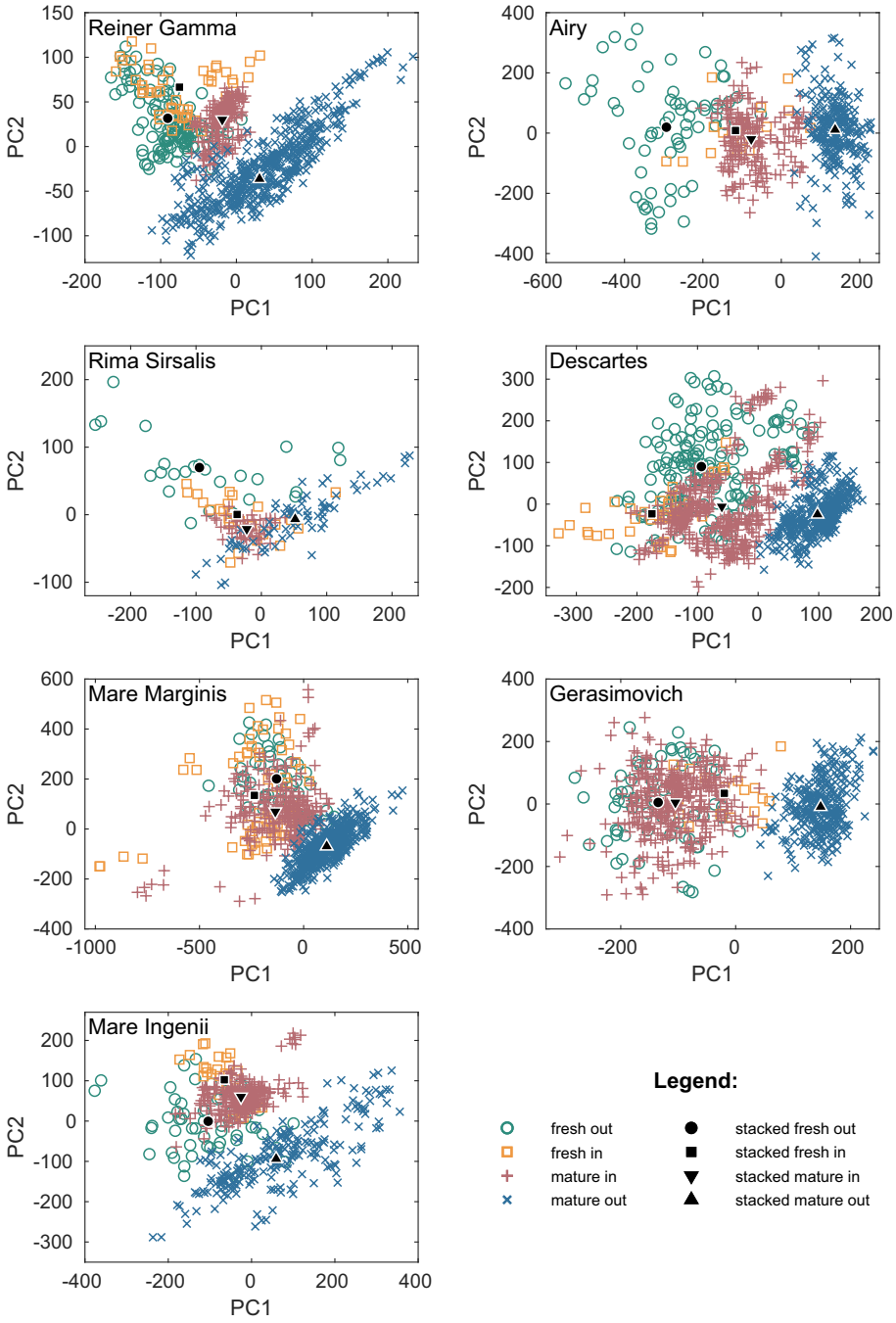

Fig. 6. A plot of the first (PC1) and second (PC2) principal component for different swirls. Black symbols represent the stacked spectra added to the statistical results.

material can diminish the non-swirl crater's albedo. Ono et al. (2009) showed, based on the Kaguya spacecraft's images, that lunar maria exhibit layered structure with depth, which can imply different mineralogies and thus different albedos of crater material compared to the surface material. Highlands are expected to be more homogeneous in this respect. Bright swirl material can also be thicker than crater material and thus support the brightness of the swirl's craters.

4.3. Interpretation of the near-/far-side dichotomy

Spectral slope did not show dichotomic behavior with respect to maria and highlands, but with respect to the near- and far-side. The Mare Marginis is on the very edge of the near side of the Moon, thus follows rather the far-side trend. The near-/far-side dichotomy can be due to the fact that near-side swirls are most exposed to the solar wind when the lunar orbit goes through the Earth's magnetotail. In contrast, far-side swirls are irradiated mainly when the Moon is outside the magnetotail. This result correlates with Trang and Lucey (2019), who claim that the magnetotail crossing is connected to a decreased production of nanophase iron particles due to lower solar wind flux.

The principal-component plots did not highlight the near-/far-side dichotomy as significantly as in the case of mare/highland dichotomy.

4.4. Comments on the statistical results

Inconclusive results appeared most often for the 1000-nm band strengths. We identified two possible reasons for this. The first may be that the results are based on a real physical phenomenon, where the

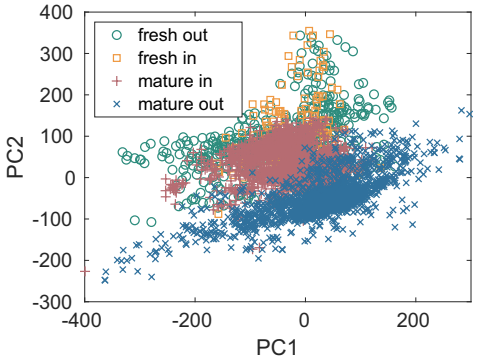

Fig. 7. A plot of the first (PC1) and second (PC2) principal component for all the swirls examined in this work. The terrains of one type have the same symbol for all the swirls.

Table 2
FeO content, in weight percent (wt%), for all seven areas of lunar swirls in this study. H = high FeO content (> 14 wt%), M = medium content (7–14 wt%), and L = low FeO content (< 7 wt%). Last column shows a rough estimate of the surface area of the swirl from which we estimated the FeO content.

swirl	FeO [wt%]	group	type	area [km^2]
Reiner Gamma	20.5	H	mare	3240
Rima Sirsalis	18.0	H	mare	680
Mare Marginis	11.5	M	mare	3660
Mare Ingenii	9.0	M	mare	4730
Airy	5.7	L	highland	4430
Descartes	5.3	L	highland	2520
Gerasimovich	2.8	L	highland	4540

mature in material really has very similar strengths of this band as either the *mature out* or fresh material. The second possibility is that the insignificance is caused by a poor description of the continuum that introduced low-order errors in the estimates of the strengths.

The Rima Sirsalis swirl's results were based on a much lower amount of data (see Section 2.1), as the swirl is small and it was difficult to find the *fresh in* and *fresh out* material in and around it. We are therefore a bit cautious about their significance, but they support our findings in the whole context.

4.5. Interpretation of stacking parameters' evolution

Similar trends to those observed in Fig. 5 had been observed earlier by Gaffey, (2010, Fig. 4). Hemingway et al. (2015) also studied the dependence of the band depth on albedo in three lunar swirls. Their results are in agreement with ours – there exists a trend from fresh impact material to darker background soils.

We saw one exception to the normal trend in our analysis: Gerasimovich's swirl material decreased the slope for the more mature material. This result is robust because we are able to see that the slope behaves in this manner even in the original data, see Fig. 4. Maybe, the *fresh out* spectra were incorrectly chosen due to the difficulties in recognizing the fresh terrains and the high variability of geology in highland regions, which is a limiting aspect of this study, as we mentioned already in Section 2.1. Furthermore, the M^3 data do not cover the whole Gerasimovich anomaly, which constrained our choice of the studied region.

The differences in the directions of inside- and outside-swirl weathering trends may be due to distinct weathering mechanisms or stages. Even Kramer et al. (2011a) saw differences between crater characteristics inside and outside swirls. More detailed spectral data from some of the upcoming missions, evaluated on more swirls, could help to uncover these trends.

We also tried to do a similar plot to Fig. 5, but with all the statistical points. This attitude did not uncover any new information, though, so we did not include the plots here.

4.6. The phase angle influence

Several authors have proposed that spectral characteristics are influenced by a viewing geometry (Carvano and Davalos, 2015). As the so-called phase angle (the Sun–target–probe orientation) increases, the albedo and slope increase as well. This phenomenon was observed for example on asteroids (Sanchez et al., 2012).

The M^3 data were subject to photometric correction, introduced by Besse et al. (2013), which corrected the Level 2 images to the standard phase angle of 30°. Although the authors admit that the correction has its simplifications and should be improved in the future, we still find the data appropriate for our research, because the trends we found are valid for each swirl separately (viewed under only one geometry). The same argument has been used by Nettles et al. (2011) for example. They suggested that spectral changes are not only a function of maturity, but local mineralogy also plays some role. Varying inclinations of trends in Fig. 5 can possibly be attributed to the different mineralogies among swirls. But specially in mare swirls, we expect the inside- and outside-swirl material to be the same (see Section 2.1), so the one-swirl data irregularities are probably caused by something else.

5. Conclusions

This work revealed differences between the mare and highland swirls. The mare/highland dichotomy was mainly observed in the plots of the first two principal components. We further noticed these trends

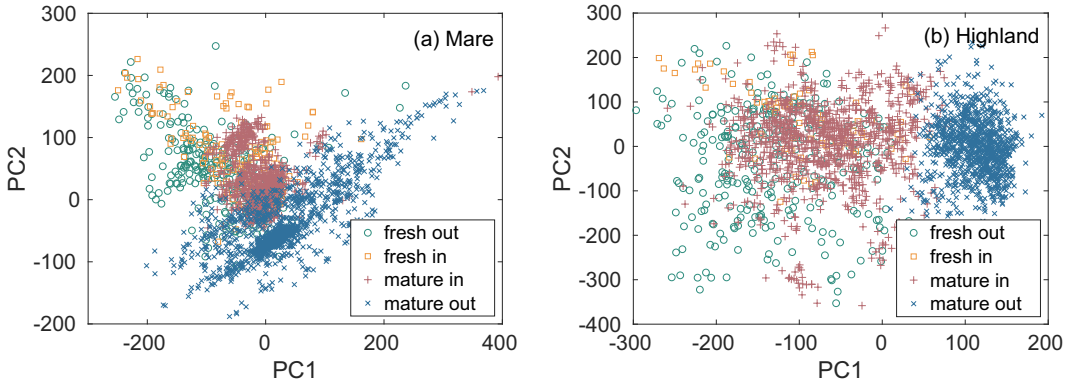

Fig. 8. A plot of the first (PC1) and second (PC2) principal component for (a) all mare swirls (Reiner Gamma, Rima Sirsalis, Mare Marginis, and Mare Ingenii), and (b) all highland swirls (Airy, Descartes, and Gerasimovich) examined in this work. The terrains of one type are plotted with the same symbol for all the swirls.

in the behavior of statistical means and stacked values of albedo and strength of the 1000-nm absorption band. We found that mare swirls have higher FeO content than highland swirls, but this is probably not the only reason for the dichotomy as there are bigger relative differences between individual mare swirls than between mare and highland swirls. The value of FeO content similar to that of lowest-FeO mare swirl or highest-FeO highland swirl used in our analysis may alternatively represent a threshold value causing the different spectral behavior of maria and highlands.

Based on the behavior of the albedo in lunar maria and strength of the 1000-nm band in lunar highlands, we see that the micrometeoroid impacts individually do not reproduce all-combined space weathering effects we observe in the unshielded regions on the Moon.

In addition, we saw the near-/far-side dichotomy in the behavior of the spectral slope, which we prescribed to the fact that the lunar orbit crosses the Earth's magnetotail, which decreases the solar wind income to the near-side swirls. This result strongly favors the solar wind stand-off hypothesis as the reason for the spectral properties of swirls.

Both, the stacking and PCA methods showed that there is a difference in the behavior of the material inside and outside the swirl. We demonstrated that the *mature in* material (swirl material distant from the fresh craters) is distinct from the fresh crater terrains, and that the *mature out* material (mature material outside the swirl formation) can always be distinguished from the other terrains in the principal component space. The behavior of the *mature in* terrain suggests that the solar wind stand-off hypothesis may be combined with a recent deposition of fresh material because micrometeoroid impacts would have weathered the surface of the swirl even without the influence of solar wind in billions years of their existence; or that the influence of micrometeoroids on the evolution of spectral parameters in lunar swirls is smaller or different than previously thought.

In future, we plan to apply our methods to asteroidal spectra, as those are thought to be influenced mainly by the solar wind (Marchi et al., 2006), which is a contrast to lunar swirls that are influenced mostly by micrometeoroid impacts. Therefore, we will be able to compare the two leading effects which cause space weathering.

Acknowledgements

We would like to thank Georgiana Kramer for her help with understanding the M^3 data and lunar spectra. We are also grateful for the comments of Ian Garrick-Bethell and an anonymous reviewer that helped to improve this manuscript.

This work was supported by the University of Helsinki Foundation, Finland and by Academy of Finland, Finland project no. 293975. The work was conducted within institutional support RVO 67985831 of the Institute of Geology of the Czech Academy of Sciences, Czech Republic.

Data availability

Datasets and source codes related to this article can be found at https://doi.org/10.5281/zenodo.1473816, hosted at zenodo.org (Chrbolková et al., 2019).

Appendix A. Online Supplementary Material

Supplementary materials to this article can be found online at https://doi.org/10.1016/j.icarus.2019.05.024.

References

Besse, S., Sunshine, J., Staid, M., Boardman, J., Pieters, C., Guasqui, P., Malaret, E., McLaughlin, S., Yokota, Y., Li, J.-Y., Jan. 2013. A visible and near-infrared photometric correction for Moon Mineralogy Mapper (M^3). Icarus 222, 229–242.

Blewett, D.T., Hawke, B.R., Lucey, P.G., Apr. 2005. Lunar optical maturity investigations: a possible recent impact crater and a magnetic anomaly. J. Geophys. Res. (Planets) 110, E04015.

Blewett, D.T., Coman, E.I., Hawke, B.R., Gillis-Davis, J.J., Purucker, M.E., Hughes, C.G., Feb. 2011. Lunar swirls: examining crustal magnetic anomalies and space weathering trends. J. Geophys. Res. (Planets) 116, E02002.

Burns, R.G., 1970. Mineralogical applications of crystal field theory. In: Electronic Spectra of Transition Metal Ions in Silicate Minerals. Cambridge University Press, Ch, pp. 83.

Burns, R.G., 1989. Spectral mineralogy of terrestrial planets: scanning their surfaces remotely. Mineral. Mag. 53.

Carvano, J.M., Davalos, J.A.G., 2015. Shape and solar phase angle effects on the taxonomic classification of asteroids. Astron. Astrophys. 580, A98.

Chrbolková, K., Kohout, T., Ďurech, J., 2019. Dataset for "Reflectance spectra of seven lunar swirls examined by statistical methods: A space weathering study". Zenodo. https://doi.org/10.5281/zenodo.1473816.

Clark, R.N., Pieters, C.M., Green, R.O., Boardman, J.W., Petro, N.E., Jun. 2011. Thermal removal from near-infrared imaging spectroscopy data of the Moon. J. Geophys. Res. (Planets) 116, E00G16.

Connolly, A.J., VanderPlas, J.T., 2014. Statistics, data mining, and machine learning in astronomy: A practical Python guide for the analysis of survey data. In: Dimensionality and its Reduction. Princeton University Press, Ch, pp. 289–302.

Deca, J., Divin, A., Lue, C., Ahmadi, T., Hornyi, M., 2018. Reiner Gamma albedo features reproduced by modeling solar wind standoff. Communications Physics 1 (1), 12.

DeMeo, F.E., Binzel, R.P., Slivan, S.M., Bus, S.J., Jul. 2009. An extension of the Bus asteroid taxonomy into the near-infrared. Icarus 202, 160–180.

Denevi, B.W., Robinson, M.S., Boyd, A.K., Sato, H., Hapke, B.W., Hawke, B.R., 2014. Characterization of space weathering from Lunar Reconnaissance Orbiter Camera ultraviolet observations of the Moon. J. Geophys. Res. (Planets) 119, 976–997.

Gaffey, M.J., 2010. Space weathering and the interpretation of asteroid reflectance spectra. Icarus 209, 564–574.

Gaffey, M.J., Burbine, T.H., Binzel, R.P., 1993. Asteroid spectroscopy - progress and perspectives. Meteoritics 28, 161–187.

Garrick-Bethell, I., Head, J.W., Pieters, C.M., 2011. Spectral properties, magnetic fields, and dust transport at lunar swirls. Icarus 212, 480–492.

Glotch, T.D., Bandfield, J.L., Lucey, P.G., Hayne, P.O., Greenhagen, B.T., Arnold, J.A., Ghent, R.R., Paige, D.A., Feb. 2015. Formation of lunar swirls by magnetic field standoff of the solar wind. Nat. Commun. 6, 6189.

Green, R.O., Pieters, C., Mouroulis, P., Eastwood, M., Boardman, J., Glavich, T., Isaacson, P., Annadurai, M., Besse, S., Barr, D., Buratti, B., Cate, D., Chatterjee, A., Clark, R., Cheek, L., Combe, J., Dhingra, D., Essandoh, V., Geier, S., Goswami, J.N., Green, R., Haemmerle, V., Head, J., Hovland, L., Hyman, S., Klima, R., Koch, T., Kramer, G., Kumar, A.S.K., Lee, K., Lundeen, S., Malaret, E., McCord, T., McLaughlin, S., Mustard, J., Nettles, J., Petro, N., Plourde, K., Racho, C., Rodriquez, J., Runyon, C., Sellar, G., Smith, C., Sobel, H., Staid, M., Sunshine, J., Taylor, L., Thaisen, K., Tompkins, S., Tseng, H., Vane, G., Varanasi, P., White, M., Wilson, D., Oct. 2011. The Moon Mineralogy Mapper (M^3) imaging spectrometer for lunar science: instrument description, calibration, on-orbit measurements, science data calibration and on-orbit validation. J. Geophys. Res. (Planets) 116, E00G19.

Hapke, B., 2001. Space weathering from Mercury to the asteroid belt. J. Geophys. Res. 106, 10039–10074.

Hemingway, D., Garrick-Bethell, I., 2012. Magnetic field direction and lunar swirl morphology: insights from Airy and Reiner Gamma. J. Geophys. Res. (Planets) 117 (E16), E10012.

Hemingway, D.J., Garrick-Bethell, I., Kreslavsky, M.A., 2015. Latitudinal variation in spectral properties of the lunar maria and implications for space weathering. Icarus 261, 66–79.

Hiroi, T., Abe, M., Kitazato, K., Abe, S., Clark, B.E., Sasaki, S., Ishiguro, M., Barnouin-Jha, O.S., 2006. Developing space weathering on the asteroid 25143 Itokawa. Nature 443, 56–58.

Hood, L.L., Artemieva, N.A., 2008. Antipodal effects of lunar basin-forming impacts: initial 3D simulations and comparisons with observations. Icarus 193, 485–502.

Hood, L.L., Schubert, G., 1980. Lunar magnetic anomalies and surface optical properties. Science 208, 49–51.

Hood, L.L., Williams, C.R., 1989. The lunar swirls - distribution and possible origins. In: Ryder, G., Sharpton, V.L. (Eds.), Lunar and Planetary Science Conference Proceedings. Vol. 19 of Lunar and Planetary Science Conference Proceedings, pp. 99–113.

Hood, L., Coleman, P.J., Wilhelms, D.E., 1979a. The moon - sources of the crustal magnetic anomalies. Science 204, 53–57.

Hood, L.L., Coleman Jr., P.J., Wilhelms, D.E., 1979b. Lunar nearside magnetic anomalies. In: Hinners, N.W. (Ed.), Lunar and Planetary Science Conference Proceedings. Vol. 10 of Lunar and Planetary Science Conference Proceedings, pp. 2235–2257.

Hood, L.L., Zakharian, A., Halekas, J., Mitchell, D.L., Lin, R.P., Acuña, M.H., Binder, A.B., 2001. Initial mapping and interpretation of lunar crustal magnetic anomalies using Lunar Prospector magnetometer data. J. Geophys. Res. 106, 27825–27840.

Ishiguro, M., Hiroi, T., Tholen, D.J., Sasaki, S., Ueda, Y., Nimura, T., Abe, M., Clark, B.E., Yamamoto, A., Yoshida, F., Nakamura, R., Hirata, N., Miyamoto, H., Yokota, Y., Hashimoto, T., Kubota, T., Nakamura, A.M., Gaskell, R.W., Saito, J., 2007. Global mapping of the degree of space weathering on asteroid 25143 Itokawa by Hayabusa/AMICA observations. Meteorit. Planet. Sci. 42, 1791–1800.

Jolliffe, I.T., 2002. Ch. Principal component analysis and factor analysis. In: Principal Component Analysis. Springer-Verlag, New York, pp. 150–166.

Jozwiak, L.M., Blewett, D.T., 2017. Geomorphological Analysis of Lunar Swirls: Insights From LROC-NAC. AGU Fall Meeting Abstracts.

Kelley, M.R., Garrick-Bethell, I., Mar. 2019. Testing the antipodal ejecta magnetization hypothesis: a closer look at the geologic setting of the lunar Gerasimovich magnetic anomalies. In: Lunar and Planetary Science Conference. Vol. 50 of Lunar and Planetary Inst. Technical Report, pp. 2071.

Klima, R.L., Pieters, C.M., Dyar, M.D., 2007. Spectroscopy of synthetic Mg-Fe pyroxenes I:

spin-allowed and spin-forbidden crystal field bands in the visible and near-infrared. Meteorit. Planet. Sci. 42, 235–253.
Kramer, G. Y., Besse, S., Dhingra, D., Nettles, J., Klima, R., Garrick-Bethell, I., Clark, R. N., Combe, J.-P., Head, III, J. W., Taylor, L. A., Pieters, C. M., Boardman, J., McCord, T. B., 2011a. M^3 spectral analysis of lunar swirls and the link between optical maturation and surface hydroxyl formation at magnetic anomalies. J. Geophys. Res. (Planets) 116, E00G18.
Kramer, G.Y., Combe, J.-P., Harnett, E.M., Hawke, B.R., Noble, S.K., Blewett, D.T., McCord, T.B., Giguere, T.A., 2011b. Characterization of lunar swirls at Mare Ingenii: a model for space weathering at magnetic anomalies. J. Geophys. Res. (Planets) 116 (E04008).
Lauretta, D.S., Balram-Knutson, S.S., Beshore, E., Boynton, W.V., Drouet d'Aubigny, C., DellaGiustina, D.N., Enos, H.L., Golish, D.R., Hergenrother, C.W., Howell, E.S., Bennett, C.A., Morton, E.T., Nolan, M.C., Rizk, B., Roper, H.L., Bartels, A.E., Bos, B.J., Dworkin, J.P., Highsmith, D.E., Lorenz, D.A., Lim, L.F., Mink, R., Moreau, M.C., Nuth, J.A., Reuter, D.C., Simon, A.A., Bierhaus, E.B., Bryan, B.H., Ballouz, R., Barnouin, O.S., Binzel, R.P., Bottke, W.F., Hamilton, V.E., Walsh, K.J., Chesley, S.R., Christensen, P.R., Clark, B.E., Connolly, H.C., Crombie, M.K., Daly, M.G., Emery, J.P., McCoy, T.J., McMahon, J.W., Scheeres, D.J., Messenger, S., Nakamura-Messenger, K., Righter, K., Sandford, S.A., 2017. OSIRIS-REx: sample return from asteroid (101955) Bennu. Space Sci. Rev. 212, 925–984.
Lawrence, D.J., Feldman, W.C., Elphic, R.C., Little, R.C., Prettyman, T.H., Maurice, S., Lucey, P.G., Binder, A.B., 2002. Iron abundances on the lunar surface as measured by the Lunar Prospector gamma-ray and neutron spectrometers. J. Geophys. Res. (Planets) 107, 5130.
Lee, J.-K., Maxwell, R., Jin, H., Baek, S.-M., Ghassemi, O., Kelley, M., Lee, H., Kim, K.-H., Lee, S., Garrick-Bethell, I., 2019. A small lunar swirl and its implications for the formation of the Reiner Gamma magnetic anomaly. Icarus 319, 869–884.
Lin, R.P., Mitchell, D.L., Curtis, D.W., Anderson, K.A., Carlson, C.W., McFadden, J., Acuna, M.H., Hood, L.L., Binder, A., Sep. 1998. Lunar surface magnetic fields and their interaction with the solar wind: results from Lunar Prospector. Science 281, 1480.
Lucey, P.G., Blewett, D.T., Jolliff, B.L., 2000. Lunar iron and titanium abundance algorithms based on final processing of Clementine ultraviolet-visible images. J. Geophys. Res. 105, 20297–20306.
Marchi, S., Paolicchi, P., Lazzarin, M., Magrin, S., 2006. A general spectral slope-exposure relation for S-type main belt and near-earth asteroids. Astron. J. 131, 1138–1141.
Matsumoto, T., Tsuchiyama, A., Miyake, A., Noguchi, T., Nakamura, M., Uesugi, K., Takeuchi, A., Suzuki, Y., Nakano, T., 2015. Surface and internal structures of a space-weathered rim of an Itokawa regolith particle. Icarus 257, 230–238.
Mikouchi, T., Komatsu, M., Hagiya, K., Ohsumi, K., Zolensky, M.E., Hoffmann, V., Martinez, J., Hochleitner, R., Kaliwoda, M., Terada, Y., Yagi, N., Takata, M., Satake, W., Aoyagi, Y., Takenouchi, A., Karouji, Y., Uesugi, M., Yada, T., 2014. Mineralogy and crystallography of some Itokawa particles returned by the Hayabusa asteroidal sample return mission. Earth, Planets, and Space 66 (82).
Neish, C.D., Blewett, D.T., Bussey, D.B.J., Lawrence, S.J., Mechtley, M., Thomson, B.J., Mini-RF Team, 2011. The surficial nature of lunar swirls as revealed by the Mini-RF instrument. Icarus 215, 186–196.
Nesvorný, D., Jedicke, R., Whiteley, R.J., Ivezić, Ž., Jan. 2005. Evidence for asteroid space weathering from the Sloan Digital Sky Survey. Icarus 173, 132–152.
Nettles, J.W., Staid, M., Besse, S., Boardman, J., Clark, R.N., Dhingra, D., Isaacson, P., Klima, R., Kramer, G., Pieters, C.M., Taylor, L.A., Jul. 2011. Optical maturity variation in lunar spectra as measured by Moon Mineralogy Mapper data. J. Geophys. Res. (Planets) 116, E00G17.
Noguchi, T., Nakamura, T., Kimura, M., Zolensky, M.E., Tanaka, M., Hashimoto, T., Konno, M., Nakato, A., Ogami, T., Fujimura, A., Abe, M., Yada, T., Mukai, T., Ueno, M., Okada, T., Shirai, K., Ishibashi, Y., Okazaki, R., 2011. Incipient space weathering observed on the surface of Itokawa dust particles. Science 333, 1121.
Nozette, S., Spudis, P., Bussey, B., Jensen, R., Raney, K., Winters, H., Lichtenberg, C.L., Marinelli, W., Crusan, J., Gates, M., Robinson, M., 2010. The Lunar Reconnaissance Orbiter Miniature Radio Frequency (mini-RF) technology demonstration. Space Sci. Rev. 150, 285–302.
Ono, T., Kumamoto, A., Nakagawa, H., Yamaguchi, Y., Oshigami, S., Yamaji, A., Kobayashi, T., Kasahara, Y., Oya, H., 2009. Lunar radar sounder observations of subsurface layers under the nearside Maria of the moon. Science 323, 909.
Pieters, C.M., Noble, S.K., 2016. Space weathering on airless bodies. J. Geophys. Res. (Planets) 121, 1865–1884.
Pieters, C.M., Taylor, L.A., Noble, S.K., Keller, L.P., Hapke, B., Morris, R.V., Allen, C.C., McKay, D.S., Wentworth, S., Sep. 2000. Space weathering on airless bodies: resolving a mystery with lunar samples. Meteorit. Planet. Sci. 35, 1101–1107.
Pinet, P.C., Shevchenko, V.V., Chevrel, S.D., Daydou, Y., Rosemberg, C., 2000. Local and regional lunar regolith characteristics at Reiner Gamma formation: optical and spectroscopic properties from Clementine and Earth-based data. J. Geophys. Res. 105, 9457–9476.
Prettyman, T.H., Hagerty, J.J., Elphic, R.C., Feldman, W.C., Lawrence, D.J., McKinney, G.W., Vaniman, D.T., 2006. Elemental composition of the lunar surface: analysis of gamma ray spectroscopy data from Lunar Prospector. J. Geophys. Res. (Planets) 111 (E10) (E12007).
Sanchez, J.A., Reddy, V., Nathues, A., Cloutis, E.A., Mann, P., Hiesinger, H., 2012. Phase reddening on near-earth asteroids: implications for mineralogical analysis, space weathering and taxonomic classification. Icarus 220, 36–50.
Schultz, P.H., Srnka, L.J., 1980. Cometary collisions on the Moon and Mercury. Nature 284, 22–26.
Shestopalov, D.I., McFadden, L.A., Golubeva, L.F., Orujova, L.O., 2010. About mineral composition of geologic units in the northern hemisphere of Vesta. Icarus 209, 575–585.
Shuai, T., Zhang, X., Zhang, L., Wang, J., 2013. Mapping global lunar abundance of plagioclase, clinopyroxene and olivine with interference imaging spectrometer hyperspectral data considering space weathering effect. Icarus 222, 401–410.
Sim, C.K., Kim, S.S., 2018. Spectral trends of the surface regolith in lunar craters. Journal of Geophysical Research (Planets) 123 (8), 2065–2075.
Sim, C.K., Kim, S.S., Lucey, P.G., Garrick-Bethell, I., Choi, Y.-J., 2017. Asymmetric space weathering on lunar crater walls. Geophys. Res. Lett. 44, 11.
Simon, S.B., Joswiak, D.J., Ishii, H.A., Bradley, J.P., Chi, M., Grossman, L., Aléon, J., Brownlee, D.E., Fallon, S., Hutcheon, I.D., Matrajt, G., McKeegan, K.D., 2008. A refractory inclusion returned by stardust from comet 81P/Wild 2. Meteorit. Planet. Sci. 43, 1861–1877.
Sturges, H.A., 1926. The choice of a class interval. J. Am. Stat. Assoc. 21 (153), 65–66.
Sunshine, J.M., Pieters, C.M., Pratt, S.F., 1990. Deconvolution of mineral absorption bands - an improved approach. J. Geophys. Res. 95, 6955–6966.
Sunshine, J.M., Pieters, C.M., Pratt, S.F., McNaron-Brown, K.S., Mar. 1999. Absorption band modeling in reflectance spectra: availability of the Modified Gaussian Model. In: Lunar and Planetary Science Conference. Lunar and Planetary Inst. Technical Report, vol. 30. pp. 1306.
Syal, M.B., Schultz, P.H., Riner, M.A., 2015. Darkening of Mercury's surface by cometary carbon. Nat. Geosci. 8, 352–356.
Trang, D., Lucey, P.G., 2019. Improved space weathering maps of the lunar surface through radiative transfer modeling of Kaguya multiband imager data. Icarus 321, 307–323.
Tsuda, Y., Yoshikawa, M., Abe, M., Minamino, H., Nakazawa, S., Oct. 2013. System design of the Hayabusa 2–asteroid sample return mission to 1999 JU3. Acta Astronautica 91, 356–362.